ACS APPLIED MATERIALS & INTERFACES

Research Article

www.acsami.org

Ultrahigh Performance Supercapacitor from Lacey Reduced Graphene Oxide Nanoribbons

Vikrant Sahu, Shashank Shekhar, Raj Kishore Sharma,* and Gurmeet Singh*

Department of Chemistry, University of Delhi, Delhi 110 007, India

Supporting Information

ABSTRACT: High performance lacey reduced graphene oxide nanoribbons (LRGONR) were chemically synthesized. Holes created during the LRGONR synthesis not only enhanced the electrolytic accessibility but destacked all the graphene layers through protrusion at edge planes and corrugation in individual graphene. LRGONR in a supercapacitor cell showed ultrahigh performance in terms of specific capacitance and capacity retention. Consistently in aqueous, nonaqueous, and ionic electrolytes, LRGONR symmetric supercapacitor exhibited exceptionally high energy/power density, typically 15.06 W h kg^{-1}/807 W kg^{-1} in aqueous at 1.7 A g^{-1}, 90 W h kg^{-1}/2046.8 W kg^{-1} in nonaqueous at 1.8 A g^{-1}, and 181.5 W h kg^{-1}/2316.8 W kg^{-1} in ionic electrolyte at ~1.6 A g^{-1}.

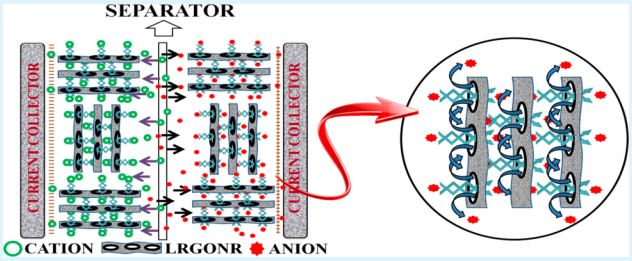

KEYWORDS: *mesoporous graphene, graphene nanoribbons, high energy and power density, supercapacitor*

INTRODUCTION

Demand for a supercapacitor as a charge storage cell is increasing mainly from portable electronic devices, electrical vehicles, and many others.[1] Extremely fast charging is a valuable feature of a supercapacitor which is possible by rapid accumulation of charges at electrode electrolyte interface (electrical double layer capacitor, EDLC).[2] High charge/discharge rates along with high energy density due to fast faradic reactions (pseudocapacitor) make this device very attractive.[3] EDLC storage takes place by the charge accumulation at electrode surface; consequently, large surface area materials like activated carbons (ACs), aerogels, carbon nanotubes, and ordered mesoporous carbons have been successfully utilized.[4] Capacitance estimation based on the assumption of a parallel plate capacitor suggests a linear relationship between specific capacitance (Csp) and surface area of the electrode. Contrary to the assumption, a large surface lies in pores, and the formation of EDL inside a pore depends on the resistance associated with electrolyte and wetting behavior of the pore surface. Hindered mass transport path, trapped air, and space constraints also significantly affect the pore accessibility. For instance, ACs (surface area ~3000 m^2 g^{-1}) in many studies have exhibited low Csp (<10 μF cm^{-2}) which is much smaller than the theoretical EDL capacitance (15−25 μF cm^{-2}). In most of the studies with ACs, only 10−20% of the theoretical specific capacitance is achieved.[5] This indicates that all the pores do not participate in charge accumulation; therefore, the material utilization/accessibility needs to be maximized for high EDL capacitance.[6,7]

Graphene with a high theoretical surface area (~2600 m^2 g^{-1}) and intrinsic specific capacitance (21 μF cm^{-2}) is an outstanding material for EDL charge storage.[8] Graphene based supercapacitor development has followed active surface area enhancement, and based on different strategies of Csp enhancement, energy density has reached 85.6 W h kg^{-1} in porous graphene ($EMIMBF_4$ ionic liquid electrolyte)[9] and 30.4 W h kg^{-1} in corrugated graphene (6 M KOH).[10] Despite the curved or porous graphene, theoretical calculation based on EDL capacitance suggests that only half of the total specific capacitance (~560 F g^{-1}; assuming EDLC as 21 μF cm^{-2} and surface area as 2675 m^2 g^{-1}) or the surface of graphene is utilized for charge storage until date.[9] A major part of graphene surface is not accessible due to stacking. Graphenes can be destacked in solution to a single sheet; however, keeping them unstacked during assembling and device application is difficult. A quick literature survey suggests that an electrode with less stacking, greater disorder, and plenty of available defect sites (edge planes) is helpful in enhancing the Csp of graphene supercapacitor.

Graphene nanoribbons (GNRs), on the other hand, have been extensively studied in recent times due to various interesting properties such as edge dependent electronic properties, and variation in band gap due to electron confinement.[11,12] Superficially, GNR is the same material; however, it exhibits better (1D) electronic conduction and has more edge planes or defect sites. Similar to graphene, GNR sheets also tend to agglomerate and restack due to van der Waals interaction.[13]

In supercapacitor electrodes, graphene has shown moderate specific capacitance (~200 F g^{-1}) due to stacking, aggregation,

Received: October 17, 2014
Accepted: January 19, 2015
Published: January 19, 2015

DOI: 10.1021/am5071706
ACS Appl. Mater. Interfaces 2015, 7, 3110−3116

and poor wetting between graphenes and electrolytes.[14] A potential solution is functionalization of graphene with hydrophilic moieties (such as −OH, −COOH),[15] or application of a polar electrolyte or surfactant assisted dispersion. These steps partially cover the graphene surface and incorporate unwanted characteristics.[16] Synthesizing graphene sheets with low stacking for high electrolytic accessibility is a challenge. Among graphene synthesis methods, mechanical cleavage, chemical vapor deposition, epitaxial growth, and graphite exfoliation[17] are sophisticated compared to solution processed reduced graphene oxide (RGO).[18] Graphene oxide (GO) synthesized from graphite powder has several drawbacks like large size of GO sheets having multilayer stacking, GO sheets being unevenly oxidized (high on outer layer and less in interlayer),[19] and graphite powder also consisting of variable electrical and mechanical properties depending on the ore it is extracted from and also inheriting various impurities.[20] We have chosen to synthesize graphene oxide nanoribbons (GONRs) by chemically unzipping the multiwalled carbon nanotubes (MWCNTs).[21] Opening all the tubes of a MWCNT is tricky, and therefore, in very recent attempts MWCNTs/GNR composites have been reported.[22,23] In order to achieve very low stacking we made finer modification to the procedure reported by Tour et.al.[21]

Due to poor conductivity and stacked graphene sheets GO is not very efficient in supercapacitor electrodes. Poor conductivity in GO is basically a result of the conversion of sp^2 hybridized carbon into sp^3 during chemical oxidation or loss of the π-conjugation.[24] Reduction of GO to regain the conductivity is carried out mainly by the processes like chemicalreduction,[25] solvothermal reduction,[26] and electrochemical reduction.[27]

In the present work lacey reduced graphene oxide nanoribbon (LRGONR) is synthesized by chemically unzipping the MWCNTs using strong oxidizing agent. As a modification, opened MWCNT is further treated with a different composition of the same set of oxidizers. This controlled treatment for 8 h was purposefully given to exaggerate the defects in nanoribbon. Prolonged oxidation, after opening the MWCNT, created random defects/holes in GONR, and thus, the edge sites are increased. Transmission electron micrographs (TEMs) taken after increasing reaction time and high temperature reduction show that the RGONR looks like lacey carbon, and we named it lacey reduced graphene oxide nanoribbon (L-RGONR). Size of these randomly distributed defects varies from 1 to 50 nm.

LRGONR symmetric supercapacitor exhibited exceptionally high energy/power density. These remarkably high values are attributed to the maximum (inter- and intralayer) graphene surface utilization. High specific capacitance obtained from LRGONR is a combined result of EDL from basal planes and pseudocapacitance from the oxygen related surface groups at the edge planes. On the basis of the structural attributes we report an ultrahigh performance supercapacitor.

EXPERIMENTAL SECTION

Synthesis of LRGONR and RGONR. A 1.5 g portion of MWCNT (NanoChina) was added in a 200 mL mixture of conc H_2SO_4 (98%):H_3PO_4 and stirred for 15 min. A 9.0 g $KMnO_4$ portion was added gradually to the H_2SO_4 dispersed MWCNT suspension, and the temperature was maintained at 80 °C. Mixture was heated for 4 + 8 h and then allowed to cool down to room temperature. MWCNT got unzipped during the first 4 h, and the extended reaction time (8 h) resulted in less stacking and hole formation in individual graphene. Furthermore, the ratio of the acids (H_2SO_4 and H_3PO_4) was adjusted to create holes, and the complete digestion was avoided.

To extract LGONR (lacey GONR), the reaction mixture was poured in 400 mL of crushed ice containing 5 mL of 30% H_2O_2. Reaction was exothermic, and a brown color viscous warm mixture was formed. After cooling, the mixture was centrifuged for 1 h at 8000 rpm. Dark brown precipitate at the bottom and semitransparent clear supernatant remained in the tube. The process was repeated 3 times so that the entire product gets precipitated. Precipitate was flocculated with 20% conc HCl and filtered with 0.45 μm PTFE membrane. Filtrate was washed with ethanol followed by DI water, and then water dispersed filtrate was sonicated and centrifuged successively. Finally, diethyl ether was added, and filtrate was sonicated. The product was filtered and kept in a vacuum desiccator. To reduce, LGONR was soaked in 6 w/w KOH and stirred for 24 h. It was kept at 600 °C for 1 h in argon. KOH was finally removed by washing with DI water until pH of the filtrate became neutral. The product was dried in vacuum oven. RGONR (reduced graphene oxide nanoribbon) was synthesized by same procedure described in Scheme 1. Step b2 was skipped, and to reduce, GONR was kept at 600 °C for 1 h (without KOH) in argon environment. Followed by this the obtained RGONR was washed with DI water and kept in vacuum oven for drying.

Scheme 1. Schematic of LRGONR Synthesis from MWCNT: (a) Pristine MWCNT, (b1) GONR Formation by Unzipping the MWCNT in 4 h, (b2) Defect Formation in GONR, and (c) High Temperature KOH Reduction and Activation

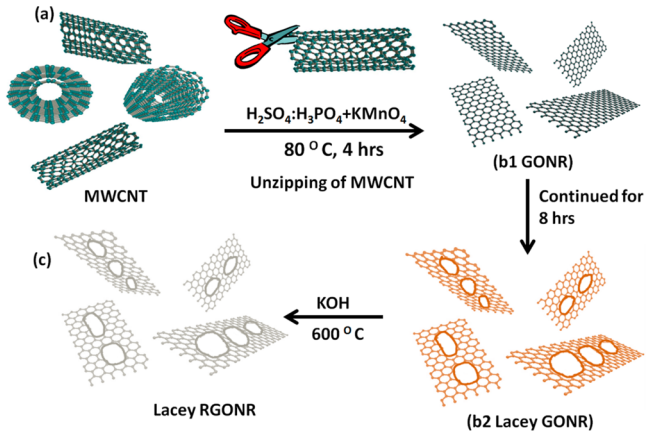

Materials Characterization. X-ray diffraction patterns of MWCNT, LGONR, and LRGONR were recorded by X-ray diffractometer (model D8 DISCOVER). Renishaw Invia Reflex Micro-Raman spectrometer was used to record Raman spectra of the samples (514 nm wavelength Ar^+ laser was used to excite the samples). BX Perkin-Elmer FTIR spectrometer was used for FTIR analysis of the sample. XPS (X-ray photoelectron spectroscopy) analysis was carried out using XPS spectrometer, Perkin-Elmer model 125. Zeiss Ultra 55 field emission scanning electron microscope and Phillips Technai T-300 transmission electron microscope were used to capture the FESEM and HRTEM images. The SSA (specific surface area), N_2 adsorption−desorption, and pore size distribution were carried on Micromeritics ASAP 2020, at 77.3 K taking nitrogen as analysis gas.

Electrochemical and Electrical Characterization. Electrochemical characteristics of the sample were recorded using CHI-604D instrument. The molar concentration of different electrolytes used was 2 M H_4SO_4, 1 M TEA BF_4 (organic electrolyte), and 1 M BMIM BF_4 (ionic liquid electrolyte)) respectively. Conductivity measurement was carried out in a low temperature cryostat attached to Keithley 2400 source meter and Keithley 651B electrometer. The galvanostatic charge−discharge tests (GCD) were carried out with PAR 4000.

DOI: 10.1021/am5071706
ACS Appl. Mater. Interfaces 2015, 7, 3110−3116

Preparation of Electrode and Supercapacitor Device. Electrodes for electrochemical measurement were fabricated by taking 5.0 mg of powder sample with 5.0 wt % nafion in isopropyl alcohol (IPA). These were ultrasonically mixed, and the formed suspension was spray deposited onto polished substrates with the help of N_2 carrier gas. Loading of the material was adjusted to 0.3−0.35 mg/cm^2. Deposited films were dried overnight in oven at 80 °C. Symmetric supercapacitor device was fabricated using two spray deposited LRGONR films of equal mass as electrodes and a nafion membrane as separator.

RESULTS AND DISCUSSION

Stepwise conversion of MWCNT to LRGONR is shown in Scheme 1a depicts a pristine MWCNT, and part b_1 shows the formation of GONR after chemical unzipping by mixture of strong oxidizers, $KMnO_4$ and conc H_2SO_4. Strong oxidizing moiety, permanganate (MnO_4^-) ion attacks the defective sites (Stone−Well sites) of MWCNT and creates further defects in axial direction leading to unzipping the MWCNT. A 4 h chemical treatment opens maximum layers of MWCNT to form GONR. Subsequent treatment for 8 h creates random holes (b_2). Since there is no preferred direction of strain in nanoribbon, MnO_4^- moiety attack takes place at a diene and continues in vicinity, taking nearly a circular shape and enlarging the defect. An 8 h treatment opened all the MWCNT layers as highly oxidized GONR with plenty of defects. Reduction and activation of LGONR in KOH (600 °C) converted it to LRGONR.

Figure 1 shows the experimental observations as proposed in Scheme 1. TEM of MWCNT shows the presence of ∼45

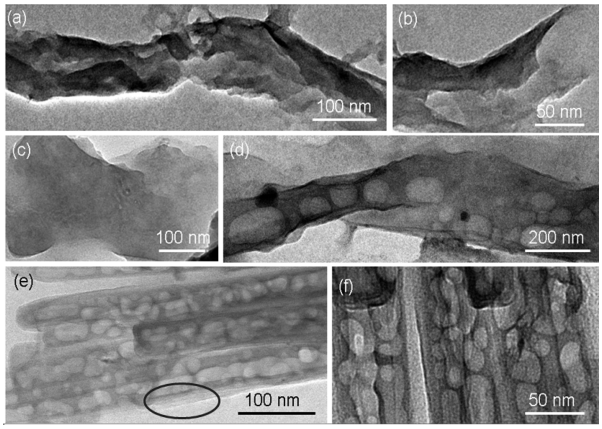

Figure 1. TEM micrographs of MWCNT unzipping and hole formation: (a) initial stage of nanotube opening in axial direction, (b) micrograph of opened MWNT tube at one end, (c) completely opened MWNT tube as stacked GONR, (d) corrugated lacey GONR after prolong chemical treatment, (e) LRGONR after high temperature reduction and activation, and (f) LRGONR showing the holes (10−50 nm) in individual graphene sheet.

concentric nanotubes (Figure S1 in Supporting Information). Average length and diameter of the MWCNTs are 2 μm and ∼35 nm, respectively. In Figure 1a, the TEM shows initial stage of MWCNT opening as the chemical moiety (MnO_4^-) attacks in axial direction along the bond strain and opens it layer by layer. Bond strain promotes the cleavage in axial direction forming nanoribbons. Figure 1b is the high resolution TEM of opened MWCNT at one end. When the reaction is continued for 4 h, MWCNT got completely unzipped in the form of 4−5 GONR stacked layers, Figure 1c. Extended treatment for 8 h to obtain further low stacking showed corrugation in GONR with formation of holes/defects of diameter 10−50 nm, Figure 1d. An 8 h treatment brought down the LGONR stacking to 3−4 layers; at some places, 2−3 layer stacking is also seen. Graphene nanoribbons got completely destacked; however, they remained entangled due to uneven and intermingled hole edges. HRTEM taken after high temperature reduction shows that the holes in LRGONR are exaggerated (Figure 1e,f). TEM analysis shows that LRGONR exists in the stacks of 2−3 graphene sheets (blue ring, Figure 1e). It is understood that the permanganate (MnO_4^-) moiety enters between two GONR layers, separating them as destacked LGONR with random hole formation, Figure 1f. The interlayer separation of individual graphene and thickness of LRGONR is discussed in Figures S2 and S3 in Supporting Information.

Figure 2a depicts the X-ray diffraction patterns (XRD) patterns of MWCNT, LGONR, and LRGONR. MWCNT

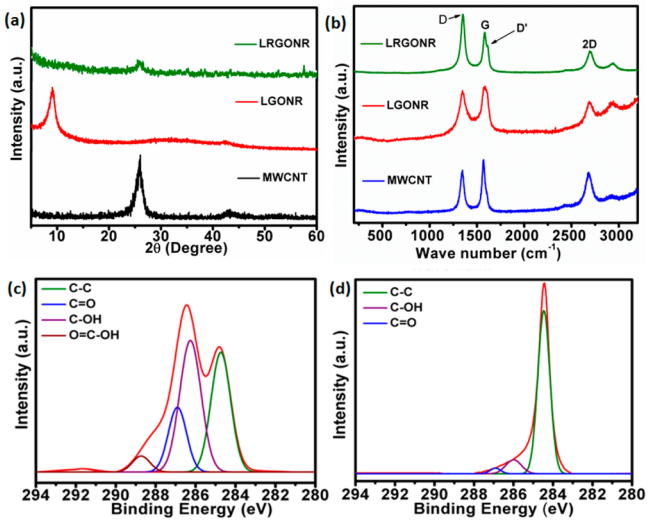

Figure 2. (a) LRGONR XRD patterns, (b) corresponding Raman spectra, (c) C 1s XPS of LGONR, and (d) C 1s XPS spectra of LRGONR.

shows an intense peak at ∼25.8° (d spacing 3.4 Å) appearing due to 002 plane stacking in coaxial tubes. In MWCNT a less intense peak at 44° appeared due to the disorder. Prominent peak at ∼10° in LGONR implicates the formation of graphene oxide, and d spacing increased to 9.6 Å which clearly indicates that all MWCNT got unzipped. In the LRGONR diffraction pattern, peak at ∼25.8° diminished significantly indicating minimal contribution from stacked graphene. The peaks at 25.8° and 44° in MWCNT diminished in intensity and disappeared, respectively, in LRGONR, suggesting the destacking of graphene layers.

Figure 2b shows the Raman spectra of MWCNT, LGONR, and LRGONR. MWCNT shows typical Raman peaks at 1370 and 1584 cm^{-1} corresponding to D and G peaks. The G peak of MWCNT is intense compared to the D peak. The I_D/I_G ratio (0.9) suggests the predominantly graphitic nature of MWCNT. Raman spectrum of LGONR shows an intense and broad D peak suggesting amorphous nature. Upon unzipping, MWCNT destacks into the layers of graphene, and due to excessive oxidation lots of defects are formed. Consequently, disorder in LGONR is substantially increased, and the D peak got intense. The I_D/I_G ratio is also increased. LRGONR spectra

DOI: 10.1021/am5071706
ACS Appl. Mater. Interfaces 2015, 7, 3110−3116

show a further intense D peak, and the ratio of the I_D/I_G peak is also increased compared to LGONR due to the clustering of the sp^2 carbon.[21] I_{2D}/I_G ratio of LGONR and LRGONR was found to be 0.75 and 0.56. The LGONR peak centered at 2691 cm^{-1}, and after KOH treatment at 600 °C the LGONR converted to LRGONR. Consequently the peak shifts to 2697.7 cm^{-1} with decrement in magnitude. The reduction of LGONR to LRGONR is also reflected in I_{2D}/I_G ratio. The XPS result is in agreement with the Raman spectra confirming the reduction of LGONR to LRGONR.[28] The 2D peak in the Raman spectra of graphene is prone to the stacked layers of graphene. The broad LRGONR peak (2697.7 cm^{-1}) is found ~19 cm^{-1} shifted to the same for monolayer graphene (2679 cm^{-1}). The shift implicates 2−4 layer stacking in LRGONR.[29] The weak shoulder in G peak is identified as D′ that indicates the disorder in the carbon lattice.[30] The band that appears at ~2935 cm^{-1} is the overtone and combination band of the E_{2g} + D peak.[31] XPS core level high resolution C 1s spectrum of both LGONR and LRGONR was recorded, and the peaks were further deconvoluted to identify different C—O functionalities present in LGONR and LRGONR (Figure 2c). Peaks at 284.7, 286.2, 286.8, and 288.7 eV correspond to the C—C, C—OH, C═O, and O═C—OH functionalities[32]in LGONR. After reduction, the C—C peak at 284.7 increased significantly due to the reduction of above surface groups in LRGONR, and spectra show only C═O and C—OH in low percentage, Figure 2d. C 1s spectra of LGONR suggest high oxidation of graphene through carbon/oxygen ratio as 1.10. This is in agreement with the XRD pattern of LGONR indicating the high oxidation. LGONR even after reduction show a significant carbon/oxygen ratio (15.6) indicating the postreduction development of oxygen related surface groups through the dangling bonds at edge planes. Carbon/oxygen ratio is significantly high in LRGONR compared to the previously reported values showing efficient reduction method.[33]

It is clear that the proposed scheme has unzipped all the MWCNT with destacking, and sufficient porosity is created in the entangled structure through holes. These noncentrosymmetric and noncocentric holes significantly reduce the van der Waals interactions in LRGONR (Figure S3 in Supporting Information). Furthermore, existence of holes in LRGONR increased the edge planes and the density of state (Figure S4 in Supporting Information).

Functionalities at defect sites possess bonds in different planes with edged carbon atom causing a protrusion at the hole circumference. Such a protrusion in LRGONR created space between two adjacent graphenes. Atomic force micrograph (AFM) in Figure 3a shows surface topology of LRGONR electrode. Depth profile in Figure 3b confirms the random holes in individual nanoribbon (depth ~0.6 nm). AFM (noncontact) image in Figure 3c shows entangled LRGONR (2−3 stacked graphene ribbons). Protrusion in underlying graphene separates it from the adjacent layer,[34,35] creating space between graphene sheets in the entangled structure. We believe that a stack of 3−4 graphene sheets form an indirect mesh like scaffold of 2D nanoribbons arranged in parallel (Figures S3 and S5 in Supporting Information). The intergraphene sheet separation is related to the level of protrusion and corrugation. It is therefore assumed that, in the plane of a nanoribbon, hole enhances vertical ion diffusibility while protrusion and corrugation in individual graphene facilitate the horizontal ion accessibility.

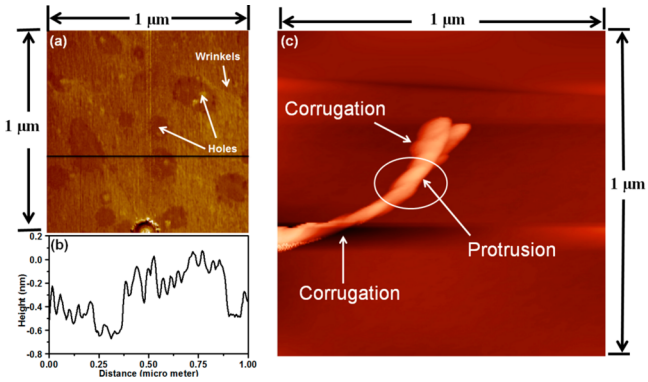

Figure 3. (a) AFM image (surface topography) of LRGONR film showing holes and wrinkles, (b) depth profile of LRGONR, (c) AFM image showing protrusion, corrugation, and twist in LRGONR.

The scanning electron micrographs of the spray deposited (a) MWCNTs and (b) GONR by unzipping the MWCNT in 4 h and (c) the LRGONR films are shown in Figure 4. Prolonged

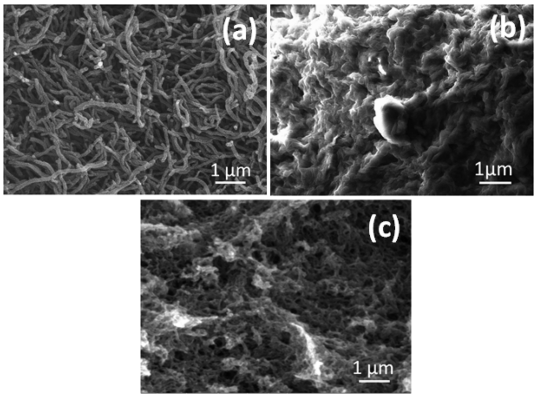

Figure 4. FESEM images of the spray deposited films (a) pristine MWCNT, (b) LGONR after 4 h unzipping of MWCNT, and (c) GONR after 12 h chemical treatment and reduction.

oxidation followed by reduction in KOH shows significant change in LRGONR character, and therefore, a distinctly porous morphology and microstructure is seen. BET surface area analysis and pore size distribution measurements in Figure 5a,b show type IV isotherm with a bottleneck type of pores in LRGONR. LRGONR specific surface area via nitrogen adsorption/desorption isotherm yielded a BET value of 190 m^2 g^{-1}. Pore distribution data of LRGONR suggest that the diameter of pores varies from 1 to 45 nm, and a majority of pores exists in >10 nm diameter. The low surface area value is attributed to the 2D defects (covering approximately 60% area,

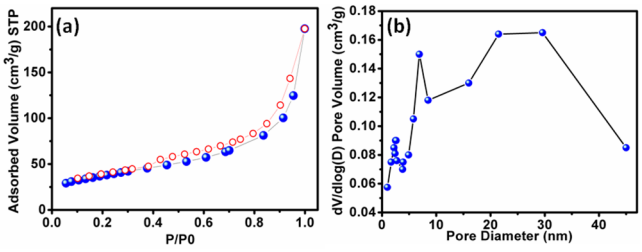

Figure 5. (a) N_2 adsorption−desorption isotherm of LRGONR and (b) pore size distribution of LRGONR.

DOI: 10.1021/am5071706
ACS Appl. Mater. Interfaces 2015, 7, 3110−3116

seen by HRTEM image) in nanoribbon; those may have deleterious effects in monolayer formation. On the contrary LGONR showed low surface area (13.5 m^2 g^{-1}) due to stacking caused by drying of solvent. The LGONR N_2 adsorption−desorption isotherm is shown in Figure S6 in Supporting Information.

Electrochemical characteristics of LRGONR (Figure 6) clearly demonstrate the superior capacitive performance

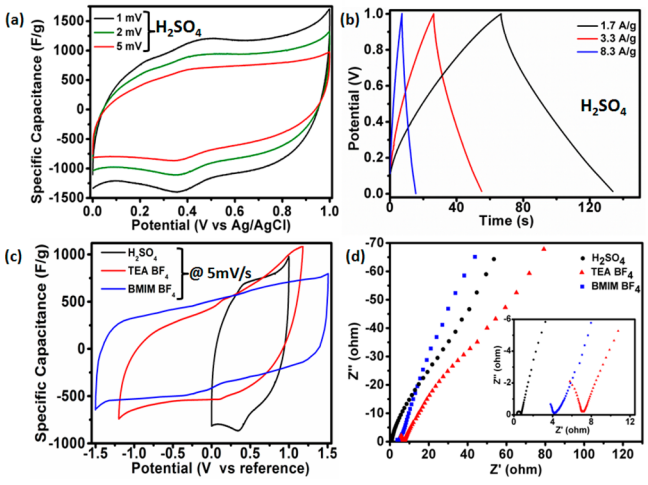

Figure 6. Electrochemical performance of LRGONR electrodes: (a) CV of LRGONR in 2 M H_2SO_4 (3 electrode cell); (b) LRGONR galvanic charge−discharge (2 electrode cell); (c) comparative CVs of LRGONR in 2 M H_2SO_4, 1.0 M TEA BF_4, and 1.0 M BMIM BF_4/AN at 5 mVs^{-1} (3 electrode cell); (d) corresponding Nyquist plot of LRGONR. Inset shows the magnified view of high frequency region (3 electrode cell).

among the majority of graphene based materials reported so far. Figure 6a shows the cyclic voltammogram (CV) of LRGONR electrode in 2.0 M H_2SO_4. CV showed mixed EDLC and pseudocapacitive characteristic with unexpectedly high Csp in three electrode cell (~1042 F g^{-1} at 1 mV s^{-1}). Voltammograms are nearly rectangular at all scan rates and shows significantly high Csp: 817 F g^{-1} at 2 mV s^{-1} and 621 F g^{-1} at 5 mV s^{-1}. The origin of high specific capacitance is further confirmed by 3 cell GCD tests (Supporting Information S-7). Csp obtained from LRGONR is quite high as compared to the previously reported corrugated graphene[10] (349 F g^{-1} at 2 mV s^{-1}), bioinspired multilayered graphene films (215.0 F g^{-1}),[36] nitrogen-doped graphene (280 F g^{-1}),[37] L-ascorbic acid reduced graphene followed by supercritical drying (128 F g^{-1}),[14] thermally reduced graphene (260.5 F g^{-1}),[38] vacuum-promoted exfoliated graphene (262 F g^{-1}),[39] self-assembled graphene/CNT hybrid films (120 F g^{-1}),[40] hydrazine vapor reduced graphene (155 F g^{-1}),[41] hierarchical graphene-carbon nanotube (326.5 F g^{-1}),[42] and reduced multilayer graphene oxide (247 F g^{-1}).[43] Furthermore, LRGONR even at a very high scan rate (700 mV s^{-1}) shows rectangular CV with high Csp and rate capability (Figure S8 in Supporting Information). Remarkably high Csp is attributed to the EDLC from basal planes of individual LRGONR and the pseudocapacitance from associated surface groups at edge planes. Consistent in LRGONR and LGONR, the origin of pseudocapacitive peaks in voltammograms (Figure 6a) indicates that some surface functionalities are undergoing redox reaction. On the contrary, XPS study shows that no significant oxygen functionalities exist in LRGONR. It is therefore assumed that, during interaction with electrolyte in CV measurement, LRGONR dangling bonds convert to pseudocapacitive surface groups. FTIR spectra of the LRGONR electrode after a few CV cycles clearly identified the presence of alcoholic, —C═O (aldehyde and ketone) at 1000−1200, 1640, and 1730 cm^{-1} functionalities (Figure S-9(b1,b2) in Supporting Information). Furthermore, the absence of redox peaks in RGONR (reduced graphene oxide nanoribbon) indicates that the pseudocapacitive surface groups are associated with edge planes of the LRGONR, and thus, the comparative CV of RGONR and LRGONR showed distinct behavior (Figure S9(a) in Supporting Information). In Figure 6b the galvanic charge−discharge (GCD) characteristic of LRGONR electrode at various current density in 2 M H_2SO_4 show that curves are nearly straight line triangle with very small IR drop. LRGONR during cycling life test in H_2SO_4 shows identical charge/discharge characterstics and highly stable performance with 97% capacity retention over 3000 GCD cycles at high current density 8.3 A g^{-1} (Figure S10 in Supporting Information).

In order to evaluate the performance with large size doping ions and operation of the LRGONR supercapacitor in wide potential window, CV investigations in nonaqueous and ionic electrolyte were carried out. We used 1 M tetra-ethyl-ammonium tetrafloroborate/acetonitrile (1 M $TEABF_4$/AN) and 1 M 1-butyl-3-methyl-imidazolium tetrafluoroborate/acetonitrile (1 M BMIM BF_4/AN) electrolyte. Figure 6c shows the comparative CV of LRGONR in three different electrolytes. Voltammograms obtained for TEA BF_4 shows nearly rectangular shape with Csp ~1272 F g^{-1}. BMIM BF_4 showed a good rectangular shaped CV in 3.0 V potential window storing ~1324 F g^{-1}. Frequency response analysis (10 mHz to 100 kHz) of LRGONR in three different electrolytes is shown in Figure 6d. The plot features a nearly vertical line, indicating a mixed EDLC and pseudocapacitive character. In high-frequency region (Figure 6d, inset), the equivalent series resistance (ESR) of LRGONR in 2 M H_2SO_4 is found below 1 Ω and little higher (~2 Ω) for TEA BF_4 and BMIM BF_4. Depending on the LRGONR/electrolyte interactions, charge transfer resistance (R_{CT}) is found to be 0.48, 2.77, and 6.3 Ω in H_2SO_4, TEA BF_4, and BMIM BF_4/AN, respectively. These results indicate that LRGONR is a low ESR and low R_{CT} electrode material. Interestingly, no Warburg resistance with large size (TEA BF_4) ions implies very low diffusion limitation. The schematic of LRGONR supercapacitor (Figure S11 in Supporting Information) depicts how the holes in LRGONR allows passage of the electrolyte ions inter- and intra-LRGONR leading to maximum graphene surface utilization. For fast charge/discharge rate and to achieve high power and energy density, ESR of an electrode plays an important role. ESR of LRGONR is found very low (0.3 Ω) which indicates good accessibility of electrolyte ions. After the ESR, small loop in the high frequency region corresponds to low electronic resistance between LRGONR,[9] and it appears due to the parallel combination of R_{CT} and EDLC.[44] No diffusion resistance in LRGONR indicates improved wettability due to the presence of oxygen related surface groups (inset Figure 6d).

GCD behavior and cycling life of LRGONR electrodes in three different electrolytes are studied in two electrode cell. The C_m determined by GCD in H_2SO_4 is found to be 115.6 F g^{-1} at 1.7 A g^{-1}, which is quite high in comparison to the recently reported data for graphene.[10,14,36−42] GCD curves of LRGONR with TEA BF_4 and BMIM BF_4 exhibited C_m as 126 (at 1.8 A

DOI: 10.1021/am5071706
ACS Appl. Mater. Interfaces 2015, 7, 3110−3116

g^{-1}) and 169.06 F g^{-1} (at 1.6 A g^{-1}) with 96.2% and 96.6% capacity retention over 3000 cycles, respectively, at 8.9 A g^{-1} in TEA BF_4 and at 8.3 A g^{-1} in BMIM BF_4. LRGONR with three different types of ions exhibited triangular shape with very small IR drop, proving the establishment of EDL with good efficiency and much less R_{CT} across the electrode (Figure S10 in Supporting Information).

CONCLUSIONS

On the basis of the improved structural attributes, LRGONR in H_2SO_4 showed a very high energy density 15.06 W h kg^{-1} at 807 W kg^{-1} power density. There is no significant decrease in energy density (8.3 W h kg^{-1}) at high power density of ~10 kW kg^{-1}. Excecptionally high energy and power density in aqueous electrolyte are attributed to the lacey structure of individual nanoribbons where the maxium graphene surface is available for ion adsorption. Similar to aqueous electrolyte the TEA BF_4 and BMIM BF_4 exhibit high performance in terms of energy and power density (Figure S12 in Supporting Information). LRGONR with TEA BF_4 electrolyte show high energy density (90 W h kg^{-1}) at 2046.8 W kg^{-1} power density, and BMIM BF_4 showed ultrahigh energy density (181.5 W h kg^{-1}) at 2316.8 W kg^{-1} power density. These values are remarkably high for any graphene based supercapacitor reported to date.

ASSOCIATED CONTENT

Supporting Information

Energy and power density calculations, HRTEM of MWCNT, HRTEM of nanoribbons showing low stacking and existence of noncocentric holes, molecular modled structure of a nanoribbon, AFM, BET and electrochemical characterization, device structure, and ragone plot. This material is available free of charge via the Internet at http://pubs.acs.org.

AUTHOR INFORMATION

Corresponding Authors

*Phone: +91 11 27666616. E-mail: drrajksharma@yahoo.co.in (R.K.S.).

*E-mail: gurmeet123@yahoo.com (G.S.).

Notes

The authors declare no competing financial interest.

ACKNOWLEDGMENTS

The authors gratefully acknowledge University of Delhi for supporting our research through various supports. Financial support from DST through sponsored research SR/S1/PC-31/2010 is gratefully acknowledged. One of the authors, V.S., especially acknowledges the SRF award from CSIR INDIA. This work is the part of the thesis of V.S.

REFERENCES

(1) Wang, G.; Zhang, L.; Zhang, J. A Review of Electrode Materials for Electrochemical Supercapacitors. *Chem. Soc. Rev.* **2012**, *41*, 797–828.

(2) Stoller, M. D.; Park, S.; Zhu, Y.; An, J.; Ruoff, R. S. Graphene-Based Ultracapacitors. *Nano Lett.* **2008**, *8*, 3498–3502.

(3) Vivekchand, S. R. C.; Rout, C. S.; Subrahmanyam, K. S.; Govindaraj, A.; Rao, C. N. R. Graphene-Based Electrochemical Supercapacitors. *J. Chem. Sci.* **2008**, *120*, 9–13.

(4) Zhang, L. L.; Zhao, X. S. Carbon-Based Materials as Supercapacitor Electrodes. *Chem. Soc. Rev.* **2009**, *38*, 2520–2531.

(5) Gryglewicz, G.; Machnikowski, J.; Lorenc-Grabowska, E.; Lotab, G.; Frackowiak, E. Effect of Pore Size Distribution of Coal-Based Activated Carbons on Double Layer Capacitance. *Electrochim. Acta* **2005**, *50*, 1197–1206.

(6) Kierzek, K.; Frackowiak, E.; Lota, G.; Gryglewicz, G.; Machnikowski, J. Electrochemical Capacitors based on Highly Porous Carbons prepared by KOH Activation. *Electrochim. Acta* **2004**, *49*, 515–523.

(7) Pandolfo, A. G.; Hollenkamp, A. F. Carbon Properties and their Role in Supercapacitors. *J. Power Sources* **2006**, *157*, 11–27.

(8) Brownson, D. A. C.; Kampouris, D. K.; Banks, C. E. Graphene Electrochemistry: Fundamental Concepts Through to Prominent Applications. *Chem. Soc. Rev.* **2012**, *41*, 6944–6976.

(9) Liu, C.; Yu, Z.; Neff, D.; Zhamu, A.; Jang, B. Z. Graphene-Based Supercapacitor with an Ultrahigh Energy Density. *Nano Lett.* **2010**, *10*, 4863–4868.

(10) Yan, J.; Liu, J.; Fan, Z.; Wei, T.; Zhang, L. High-Performance Supercapacitor Electrodes based on highly Corrugated Graphene Sheets. *Carbon* **2012**, *50*, 2179–2188.

(11) Li, X.; Wang, X.; Zhang, L.; Lee, S.; Dai, H. Ultrasmooth Graphene Nanoribbon Semiconductors. *Science* **2008**, *319*, 1229–1232.

(12) Wang, X.; Li, X.; Zhang, L.; Yoon, Y.; Weber, P. K.; Wang, H.; Guo, J.; Dai, H. Doping of Graphene through Electrothermal Reactions with Ammonia. *Science* **2009**, *324*, 768–771.

(13) Li, D.; Muller, M. B.; Gilje, S.; Kaner, R. B.; Wallace, G. G. Processable Aqueous Dispersions of Graphene Nanosheets. *Nat. Nanotechnol.* **2008**, *3*, 101–105.

(14) Zhang, X.; Sui, Z.; Xu, B.; Yue, S.; Luo, Y.; Zhan, W.; Liu, B. Mechanically Strong and Highly Conductive Graphene Aerogel and Its Use as Electrodes for Electrochemical Power Sources. *J. Mater. Chem.* **2011**, *21*, 6494–6497.

(15) Wang, H.; Hao, Q.; Yang, X.; Lu, L.; Wang, X. Graphene Oxide Doped Polyaniline for Supercapacitors. *Electrochem. Commun.* **2009**, *11*, 1158–1161.

(16) Lei, Z.; Christov, N.; Zhao, X. S. Intercalation of Mesoporous Carbon Spheres between Reduced Graphene Oxide Sheets for Preparing High-Rate Supercapacitor Electrodes. *Energy Environ. Sci.* **2011**, *4*, 1866–1873.

(17) Guo, S.; Dong, S. Graphene Nanosheet: Synthesis, Molecular Engineering, Thin Film, Hybrids, and Energy and Analytical Applications. *Chem. Soc. Rev.* **2011**, *40*, 2644–2672.

(18) Wu, D.; Zhang, F.; Liang, H.; Feng, X. Nanocomposites and Macroscopic Materials: Assembly of Chemically Modified Graphene Sheets. *Chem. Soc. Rev.* **2012**, *41*, 6160–6177.

(19) Zhang, L. L.; Zhou, R.; Zhao, X. S. Graphene-Based Materials as Supercapacitor Electrodes. *J. Mater. Chem.* **2010**, *20*, 5983–5992.

(20) Wissler, M. Graphite and Carbon Powders for Electrochemical Applications. *J. Power Sources* **2006**, *156*, 142–150.

(21) Kosynkin, D. V.; Higginbotham, A. L.; Sinitskii, A.; Lomeda, J. R.; Dimiev, A.; Price, B. K.; Tour, J. M. Longitudinal Unzipping of Carbon Nanotubes to form Graphene Nanoribbons. *Nature* **2009**, *458*, 872–876.

(22) Lin, L.-Y.; Yeh, M.-H.; Tsai, J.-T.; Huang, Y.-H.; Sun, C.-L.; Ho, K.-C. A Novel Core–Shell Multi-Walled Carbon Nanotube@Graphene Oxide Nanoribbon Heterostructure as a Potential Supercapacitor Material. *J. Mater. Chem. A* **2013**, *1*, 11237–11245.

(23) Wang, H.; Wang, Y.; Hu, Z.; Wang, X. Cutting and Unzipping Multiwalled Carbon Nanotubes into Curved Graphene Nanosheets and Their Enhanced Supercapacitor Performance. *ACS Appl. Mater. Interfaces* **2012**, *4*, 6827–6834.

(24) Dreyer, D. R.; Park, S.; Bielawski, C. W.; Ruoff, R. S. The Chemistry of Graphene Oxide. *Chem. Soc. Rev.* **2010**, *39*, 228–240.

(25) Stankovich, S.; Dikin, D. A.; Piner, R. D.; Kohlhaas, K. A.; Kleinhammes, A.; Jia, Y.; Wu, Y.; Nguyen, S. T.; Ruoff, R. S. Synthesis of Graphene-Based Nanosheets via Chemical Reduction of Exfoliated Graphite Oxide. *Carbon* **2007**, *45*, 1558–1565.

(26) Dubin, S.; Gilje, S.; Wang, K.; Tung, V. C.; Cha, K.; Hall, A. S.; Farrar, J.; Varshneya, R.; Yang, Y.; Kaner, R. B. A One-Step,

DOI: 10.1021/am5071706
ACS Appl. Mater. Interfaces 2015, 7, 3110–3116

Solvothermal Reduction Method for Producing Reduced Graphene Oxide Dispersions in Organic Solvents. *ACS Nano* **2010**, *4*, 3845−3852.
(27) Shao, Y.; Wang, J.; Engelhard, M.; Wang, C.; Lin, Y. Facile and Controllable Electrochemical Reduction of Graphene Oxide and Its Applications. *J. Mater. Chem.* **2010**, *20*, 743−748.
(28) Yang, D.; Velamakanni, A.; Bozoklu, G.; Park, S.; Stoller, M.; Piner, R. D.; Stankovich, S.; Jung, I.; Field, D. A.; Ventrice, C. A., Jr.; Ruoff, R. S. Chemical Analysis of Graphene Oxide Films after Heat and Chemical Treatments by X-ray Photoelectron and Micro-Raman Spectroscopy. *Carbon* **2009**, *47*, 145−152.
(29) Akhavan, O.; Ghaderi, E.; Emamy, H. Nontoxic Concentrations of PEGylated Graphene Nanoribbons for Selective Cancer Cell Imaging and Photothermal Therapy. *J. Mater. Chem.* **2012**, *22*, 20626−20633.
(30) Wu, K.-H.; Wang, D.-W.; Gentle, I. R. Revisiting Oxygen Reduction Reaction on Oxidized and Unzipped Carbon Nanotubes. *Carbon* **2015**, *81*, 295−304.
(31) Wang, Y.; Alsmeyer, D. C.; McCreery, R. L. Raman Spectroscopy of Carbon Materials: Structural Basis of Observed Spectra. *Chem. Mater.* **1990**, *2*, 557−563.
(32) Pei, S.; Zhao, J.; Du, J.; Ren, W.; Cheng, H.-M. Direct Reduction of Graphene Oxide Films into Highly Conductive and Flexible Graphene Films by Hydrohalic Acids. *Carbon* **2010**, *48*, 4466−4474.
(33) Akhavan, O. The effect of Heat Treatment on Formation of Graphene Thin Films from Graphene Oxide Nanosheets. *Carbon* **2010**, *48*, 509−519.
(34) Sinitskii, A.; Kosynkin, D. V.; Dimiev, A.; Tour, J. M. Corrugation of Chemically Converted Graphene Monolayers on SiO_2. *ACS Nano* **2010**, *4*, 3095−3102.
(35) Ugeda, M. M.; Brihuega, I.; Guinea, F.; Gomez-Rodriguez, J. M. Missing Atom as a Source of Carbon Magnetism. *Phys. Rev. Lett.* **2010**, *104*, 096804.
(36) Yang, X.; Zhu, J.; Qiu, L.; Li, D. Bioinspired Effective Prevention of Restacking in Multilayered Graphene Films: Towards the Next Generation of High-Performance Supercapacitors. *Adv. Mater.* **2011**, *23*, 2833−2838.
(37) Jeong, H. M.; Lee, J. W.; Shin, W. H.; Choi, Y. J.; Shin, H. J.; Kang, J. K.; Choi, J. W. Nitrogen-Doped Graphene for High-Performance Ultracapacitors and the Importance of Nitrogen-Doped Sites at Basal Planes. *Nano Lett.* **2011**, *11*, 2472−2477.
(38) Zhao, B.; Liu, P.; Jiang, Y.; Pan, D.; Tao, H.; Song, J.; Fang, T.; Xu, W. Supercapacitor Performances of Thermally Reduced Graphene Oxide. *J. Power Sources* **2012**, *198*, 423−427.
(39) Lv, W.; Tang, D.-M.; He, Y.-B.; You, C.-H.; Shi, Z.-Q; Chen, X.-C.; Chen, C.-M.; Hou, P.-X.; Liu, C.; Yang, Q.-H. Low-Temperature Exfoliated Graphenes: Vacuum-Promoted Exfoliation and Electrochemical Energy Storage. *ACS Nano* **2009**, *3*, 3730−3736.
(40) Yu, D.; Dai, L. Self-Assembled Graphene/Carbon Nanotube Hybrid Films for Supercapacitors. *J. Phys. Chem. Lett.* **2010**, *1*, 467−470.
(41) Dong, X.; Xing, G.; Chan.-Park, M. B.; Shi, W.; Xiao, N.; Wang, J.; Yan, Q.; Sum, T. C.; Huang, W.; Chen, P. The Formation of a Carbon Nanotube−Graphene Oxide Core−Shell Structure and Its Possible Applications. *Carbon* **2011**, *49*, 5071−5078.
(42) Yang, S. Y.; Chang, K. H.; Tien, H. W.; Lee, Y. F.; Li, S. M.; Wang, Y. S.; Wang, J. Y.; Ma, C.C. M.; Hu, C.-C. Design and Tailoring of a Hierarchical Graphene-Carbon Nanotube Architecture for Supercapacitors. *J. Mater. Chem.* **2011**, *21*, 2374−2380.
(43) Yoo, J. J.; Balakrishnan, K.; Huang, J.; Meunier, V.; Sumpter, B. G.; Srivastava, A.; Conway, M.; Reddy, A. L. M.; Yu, J.; Robert, V.; Ajayan, P. M. Ultrathin Planar Graphene Supercapacitors. *Nano Lett.* **2011**, *11*, 1423−1427.
(44) Kim, T. Y.; Lee, H. W.; Stoller, M.; Dreyer, D. R.; Bielawski, C. W.; Ruoff, R. S.; Suh, K. S. High-Performance Supercapacitors Based on Poly(ionic liquid)-Modified Graphene Electrodes. *ACS Nano* **2010**, *5*, 436−442.

DOI: 10.1021/am5071706
ACS Appl. Mater. Interfaces 2015, 7, 3110−3116